Engineering Fracture Mechanics 93 (2012) 239–262

Contents lists available at SciVerse ScienceDirect

Engineering Fracture Mechanics

journal homepage: www.elsevier.com/locate/engfracmech

Computational implementation of the PPR potential-based cohesive model in ABAQUS: Educational perspective

Kyoungsoo Park [a,*], Glaucio H. Paulino [b]

[a] School of Civil & Environmental Engineering, Yonsei University, 50 Yonsei-ro, Seodaemun-gu, Seoul, Republic of Korea
[b] Department of Civil & Environmental Engineering, University of Illinois at Urbana–Champaign, 205 North Mathews Ave., Urbana, IL 61801, United States

ARTICLE INFO

Article history:
Received 2 August 2011
Received in revised form 9 February 2012
Accepted 9 February 2012

Keywords:
Cohesive zone model
PPR potential-based model
Crack propagation
Cohesive element

ABSTRACT

A potential-based cohesive zone model, so called the PPR model, is implemented in a commercial software, e.g. ABAQUS, as a user-defined element (UEL) subroutine. The intrinsic cohesive zone modeling approach is employed because it can be formulated within the standard finite element framework. The implementation procedure for a two-dimensional linear cohesive element and the algorithm for the PPR potential-based model are presented in-detail. The source code of the UEL subroutine is provided in Appendix for educational purposes. Three computational examples are investigated to verify the PPR model and its implementation. The computational results of the model agree well with the analytical solutions.

1. Introduction

The cohesive zone model has been a powerful concept to approximate nonlinear fracture processes [1,2]. The concept of the cohesive zone model was presented by Barenblatt [3] and Dugdale [4]. Since then, the model has been utilized to investigate a wide range of failure phenomena, which include, for example, fracture of quasi-brittle materials [5–8], bond-slip in reinforced concrete [9], delamination in adhesive bond joints [10,11], and matrix/particle debonding [12–14].

One of essential aspects in the cohesive zone model is the choice of a traction–separation relation. Because most traction–separation relationships display limitations, especially under mixed-mode conditions, the relationship should be selected with great caution [15]. Among various traction–separation relationships, the so-called PPR potential based model demonstrates the consistency of the constitutive relationship under mixed-mode conditions while considering different fracture energies with respect to fracture modes [15]. In order to benefit from the PPR potential-based model and capabilities of existing commercial softwares for nonlinear fracture analysis, one could develop a user-defined element (UEL) subroutine for the PPR model in a commercial software such as ABAQUS [16].

Computational implementation of an existing algorithm (or model) may be a challenging task, especially for beginners in a new research area, because the detailed procedure or source codes are not generally provided in scientific journal papers. However, in order to facilitate research and to benefit from existing scientific contributions for researchers and engineers, there are several papers which address computational implementations. For instance, Sigmund [17] presented an implementation of a topology optimization code for compliance minimization of statically loaded structures. Giner et al. [18] demonstrated an ABAQUS implementation of the extended finite element method as a UEL subroutine for linear elastic fracture analysis.

* Corresponding author. Tel.: +82 2 2123 5806; fax: +82 2 364 5300.
E-mail address: k-park@yonsei.ac.kr (K. Park).

0013-7944/$ - see front matter © 2012 Elsevier Ltd. All rights reserved.
http://dx.doi.org/10.1016/j.engfracmech.2012.02.007

Nomenclature

a_p	radius of particle
$\boldsymbol{B}_c$	global displacement–separation relation matrix
$\boldsymbol{D}_c$	material tangent stiffness matrix of the cohesive zone model
E^m, E^p	elastic moduli of matrix and particle
f	volume fraction of particle
$\boldsymbol{f}_{coh}$	internal force vector of a cohesive surface element
$\boldsymbol{K}_{coh}$	tangent matrix of a cohesive surface element
$\boldsymbol{L}$	local displacement–separation relation matrix
m, n	nondimensional exponents in the PPR model
$\boldsymbol{N}$	shape functional matrix
$\boldsymbol{R}$	rotational matrix of nodal displacements
$\boldsymbol{T}_c$	cohesive traction vector
$\boldsymbol{T}_{ext}$	external traction vector
T_n, T_t	normal and tangential cohesive tractions
T_n^{υ}, T_n^{υ}	normal and tangential cohesive tractions for the unloading/reloading relation
$\boldsymbol{u}$	displacement field
$\bar{\boldsymbol{u}}$	nodal displacement vector in the global coordinates
$\tilde{\boldsymbol{u}}$	nodal displacement vector in the local coordinates
$\boldsymbol{x}$	local coordinates
$\boldsymbol{X}$	global coordinates
α, β	shape parameters in the PPR model
α_{υ}, β_{υ}	shape parameters in the unloading/reloading relation
Γ	boundary of external traction
Γ_c	boundary of cohesive fracture surface
Γ_n, Γ_t	energy constants in the PPR model
δ_n, δ_t	normal and tangential final crack opening widths
δ_{nc}, δ_{tc}	normal and tangential critical opening displacements
$\bar{\delta}_n$, $\bar{\delta}_t$	normal and tangential conjugate final crack opening widths
$\boldsymbol{\Delta}$	separation field in the local coordinates
$\tilde{\boldsymbol{\Delta}}$	nodal separation vector in the local coordinates
Δ_n, Δ_t	normal and tangential separations along fracture surface
$\Delta_{n_{\max}}$, $\Delta_{t_{\max}}$	maximum normal and tangential separations in a loading history
$\bar{\epsilon}$	macroscopic strain
θ	angle between the global coordinates and the local coordinates
$\boldsymbol{\epsilon}$	Cauchy strain
λ_n, λ_t	initial slope indicators in the PPR model
$\boldsymbol{\Lambda}$	coordinate transformation matrix
ν^m, ν^p	Poisson's ratios of matrix and particle
$\bar{\sigma}$	macroscopic stress
$\bar{\sigma}^p$	average stress in particle
$\boldsymbol{\sigma}$	Cauchy stress
$\sigma_{\max}$, $\tau_{\max}$	normal and tangential cohesive strengths
ϕ_n, ϕ_t	normal and tangential fracture energies
Ψ	potential function for cohesive fracture
Ω	domain
$\langle \cdot \rangle$	Macauley bracket

The present paper focuses on the implementation of the PPR potential-based cohesive zone model in ABAQUS as a UEL subroutine. The UEL subroutine is provided in Appendix for educational purposes. Notice that the finite element-based intrinsic cohesive zone modeling approach is employed because it can be easily implemented in an existing standard finite analysis code. Furthermore, the PPR model can also be implemented in conjunction with other computational techniques such as extrinsic cohesive zone modeling [19,20], extended/generalized finite element method (XFEM/GFEM) [21,22], and embedded discontinuities [23–25]. However, as indicated above, the intrinsic model is the approach of choice in this paper.

The remainder of the paper is organized as follows. The formulation of cohesive elements and the PPR potential based model are explained in the following section. Then, Section 3 presents the computational implementation of the PPR potential-based model for a two-dimensional linear cohesive element. Section 4 investigates three examples: simple patch test, mixed-mode bending test and matrix/particle debonding. Finally, the paper is summarized in Section 5.

2. Cohesive zone model

The cohesive zone model mitigates stress singularity in linear elastic fracture mechanics, and represents the nonlinear fracture process zone ahead of a crack tip, as illustrated in Fig. 1. The cohesive crack propagation may consist of four stages: elastic, initiation, softening and complete failure [26,27]. The intrinsic cohesive zone modeling approach also includes the four stages, and thus the model can be implemented within a standard finite element framework. For the constitutive relationship of cohesive fracture, the PPR potential-based model is utilized in conjunction with an unloading/reloading relation, as discussed in the following subsections.

2.1. Finite element formulation

The weak form of the governing equation is obtained from the principle of virtual work. The summation of the virtual strain energy in the domain (Ω) and the cohesive fracture energy evaluated on the fracture surface (Γ_c) is equal to the virtual work done by external traction ($\boldsymbol{T}_{ext}$) on boundary (Γ)

$$\int_{\Omega} \delta\boldsymbol{\epsilon} : \boldsymbol{\sigma} dV + \int_{\Gamma_c} \delta\boldsymbol{\Delta} \cdot \boldsymbol{T}_c \, dS = \int_{\Gamma} \delta\boldsymbol{u} \cdot \boldsymbol{T}_{ext} \, dS \tag{1}$$

where $\delta\boldsymbol{\epsilon}$, $\delta\boldsymbol{u}$ and $\delta\boldsymbol{\Delta}$ are virtual strain, virtual displacement and virtual separation, respectively. In addition, $\boldsymbol{\sigma}$ is stress tensor in the deformed configuration (i.e. Cauchy stress), while $\boldsymbol{T}_c$ is cohesive traction along the fracture surface. The first term in the left hand side of Eq. (1) is associated with the internal force of volumetric elements (or bulk elements), while the second term is related to the internal cohesive force of cohesive surface elements. The term in the right hand side of Eq. (1) corresponds to the external force.

The domain (Ω) is discretized into finite elements, and the displacement field ($\boldsymbol{u}$) is approximated by interpolating the nodal displacement ($\bar{\boldsymbol{u}}$) with shape functions,

$$\boldsymbol{u}(\boldsymbol{X}) = \boldsymbol{N}\bar{\boldsymbol{u}} \tag{2}$$

where $\boldsymbol{N}$ is a shape function matrix, and $\boldsymbol{X}$ denotes the global coordinates.

In addition, the local separation ($\boldsymbol{\Delta}$) is approximated by using the nodal displacement ($\bar{\boldsymbol{u}}$). In order to obtain the local separation based on the global nodal displacement, the global coordinates ($\boldsymbol{X}$) are first transformed to the local coordinates ($\boldsymbol{x}$) of a cohesive element, i.e.

$$\boldsymbol{x} = \boldsymbol{\Lambda}\boldsymbol{X} \tag{3}$$

where $\boldsymbol{\Lambda}$ is a coordinate transformation matrix. Similarly, the global nodal displacement ($\bar{\boldsymbol{u}}$) is transformed to the local nodal displacement ($\tilde{\boldsymbol{u}}$) by a rotational matrix ($\boldsymbol{R}$),

$$\tilde{\boldsymbol{u}} = \boldsymbol{R}\bar{\boldsymbol{u}} \tag{4}$$

where $\boldsymbol{R}$ consists of a coordinate transformation matrix ($\boldsymbol{\Lambda}$). An example of $\boldsymbol{R}$ for a two-dimensional linear cohesive element is provided in Section 3.1. From the local nodal displacement, one obtains the local nodal displacement jump, or separation, ($\tilde{\boldsymbol{\Delta}}$) along the surface normal and tangential directions, i.e. the relationship between nodal displacements and nodal separation

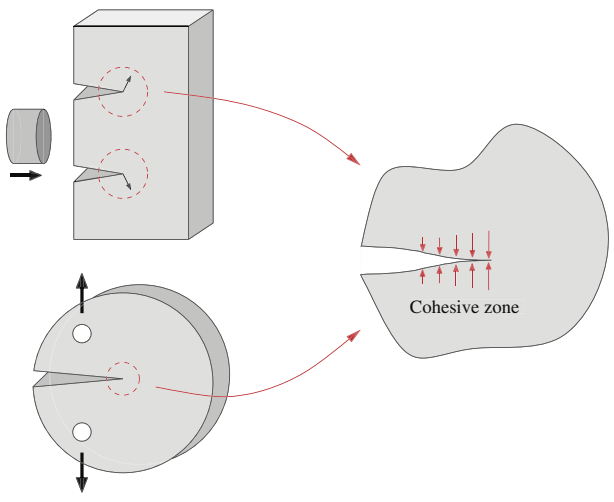

Fig. 1. Illustration of the cohesive zone modeling concept.

$$\widetilde{\boldsymbol{\Delta}} = \boldsymbol{L}\tilde{\boldsymbol{u}} \tag{5}$$

where $\boldsymbol{L}$ is a local displacement–separation relation matrix. Then, separation ($\boldsymbol{\Delta}(\boldsymbol{x})$) along a cohesive surface element is interpolated from the nodal separation by using shape functions,

$$\boldsymbol{\Delta}(\boldsymbol{x}) = \boldsymbol{N}\widetilde{\boldsymbol{\Delta}}. \tag{6}$$

Finally, the substitution of Eqs. (4) and (5) into Eq. (6) leads to the relationship between the local separation and the global nodal displacement, i.e.

$$\boldsymbol{\Delta}(\boldsymbol{x}) = \boldsymbol{B}_c\bar{\boldsymbol{u}} \tag{7}$$

where $\boldsymbol{B}_c$ is a global displacement–separation relation matrix (i.e. $\boldsymbol{B}_c = \boldsymbol{NLR}$).

Based on the approximated displacement field, the internal force vector ($\boldsymbol{f}_{coh}$) of a cohesive surface element is given as

$$\boldsymbol{f}_{coh} = \int_{\Gamma_c} \boldsymbol{B}_c^T \boldsymbol{T}_c \, dS. \tag{8}$$

The gradient of the internal cohesive force vector leads to the tangent matrix ($\boldsymbol{K}_{coh}$) of a cohesive surface element, i.e.

$$\boldsymbol{K}_{coh} = \frac{\partial \boldsymbol{f}_{coh}}{\partial \bar{\boldsymbol{u}}} = \int_{\Gamma_c} \boldsymbol{B}_c^T \frac{\partial \boldsymbol{T}_c}{\partial \boldsymbol{\Delta}} \frac{\partial \boldsymbol{\Delta}}{\partial \bar{\boldsymbol{u}}} \, dS = \int_{\Gamma_c} \boldsymbol{B}_c^T \frac{\partial \boldsymbol{T}_c}{\partial \boldsymbol{\Delta}} \boldsymbol{B}_c \, dS. \tag{9}$$

Note that $\boldsymbol{T}_c$ and $\partial \boldsymbol{T}_c/\partial \boldsymbol{\Delta}$ are obtained from the PPR potential-based cohesive zone model, as presented in the following subsection. In addition, the formulation is applicable for both two- and three-dimensional finite element implementations. The implementation procedure of a two-dimensional linear cohesive element is discussed in Section 3.

2.2. PPR Potential-based cohesive zone model

The cohesive traction–separation relationship is obtained from a potential-based cohesive zone model, so-called the PPR model [15,1]. The potential of cohesive fracture is given by

$$\Psi(\Delta_n, \Delta_t) = \min(\phi_n, \phi_t) + \left[\Gamma_n\left(1 - \frac{\Delta_n}{\delta_n}\right)^{\alpha}\left(\frac{m}{\alpha} + \frac{\Delta_n}{\delta_n}\right)^{m} + \langle \phi_n - \phi_t \rangle\right]\left[\Gamma_t\left(1 - \frac{|\Delta_t|}{\delta_t}\right)^{\beta}\left(\frac{n}{\beta} + \frac{|\Delta_t|}{\delta_t}\right)^{n} + \langle \phi_t - \phi_n \rangle\right]. \tag{10}$$

where $\langle \cdot \rangle$ is the *Macauley bracket*, i.e.

$$\langle x \rangle = \begin{cases} 0, & (x \leqslant 0) \\ x, & (x > 0). \end{cases} \tag{11}$$

Because of the nature of the potential, the derivatives of the PPR potential with respect to the normal and tangential separations lead to the normal and tangential cohesive tractions,

$$\begin{aligned} T_n(\Delta_n, \Delta_t) &= \frac{\Gamma_n}{\delta_n}\left[m\left(1 - \frac{\Delta_n}{\delta_n}\right)^{\alpha}\left(\frac{m}{\alpha} + \frac{\Delta_n}{\delta_n}\right)^{m-1} - \alpha\left(1 - \frac{\Delta_n}{\delta_n}\right)^{\alpha-1}\left(\frac{m}{\alpha} + \frac{\Delta_n}{\delta_n}\right)^{m}\right] \\ &\quad \left[\Gamma_t\left(1 - \frac{|\Delta_t|}{\delta_t}\right)^{\beta}\left(\frac{n}{\beta} + \frac{|\Delta_t|}{\delta_t}\right)^{n} + \langle \phi_t - \phi_n \rangle\right], \\ T_t(\Delta_n, \Delta_t) &= \frac{\Gamma_t}{\delta_t}\left[n\left(1 - \frac{|\Delta_t|}{\delta_t}\right)^{\beta}\left(\frac{n}{\beta} + \frac{|\Delta_t|}{\delta_t}\right)^{n-1} - \beta\left(1 - \frac{|\Delta_t|}{\delta_t}\right)^{\beta-1}\left(\frac{n}{\beta} + \frac{|\Delta_t|}{\delta_t}\right)^{n}\right] \\ &\quad \left[\Gamma_n\left(1 - \frac{\Delta_n}{\delta_n}\right)^{\alpha}\left(\frac{m}{\alpha} + \frac{\Delta_n}{\delta_n}\right)^{m} + \langle \phi_n - \phi_t \rangle\right]\frac{\Delta_t}{|\Delta_t|}, \end{aligned} \tag{12}$$

respectively. Notice that the normal and tangential tractions satisfy basic symmetry and anti-symmetry requirements (with respect to Δ_t), i.e. $T_n(\Delta_n, \Delta_t) = T_n(\Delta_n, -\Delta_t)$ and $T_t(\Delta_n, \Delta_t) = -T_t(\Delta_n, -\Delta_t)$. The value of $T_t(\Delta_n, \Delta_t)$ at $\Delta_t = 0$ exists in the limit sense. In addition, the PPR potential is defined within a cohesive interaction region. If separation is outside of the interaction region, the cohesive traction is equal to zero.

The PPR potential-based model satisfies the following boundary conditions associated with cohesive fracture.

- The complete normal separation occurs ($T_n = 0$) when either normal or tangential separation reaches a certain length scale,

$$T_n(\delta_n, \Delta_t) = 0, \quad T_n(\Delta_n, \bar{\delta}_t) = 0, \tag{13}$$

  where δ_n is a normal final crack opening width, and $\bar{\delta}_t$ is a tangential conjugate final crack opening width.
- Similarly, the complete tangential separation occurs ($T_t = 0$) when either normal or tangential separation reaches a certain length scale,

$$T_t(\bar{\delta}_n, \Delta_t) = 0, \quad T_t(\Delta_n, \delta_t) = 0. \tag{14}$$

where $\bar{\delta}_n$ is a normal conjugate final crack opening width, and δ_t is a tangential final crack opening width.

- The area under the pure normal and tangential traction–separation curves provides the fracture energy in the normal (ϕ_n) and tangential (ϕ_t) directions, respectively,

$$\phi_n = \int_0^{\delta_n} T_n(\Delta_n, 0)\mathrm{d}\Delta_n, \quad \phi_t = \int_0^{\delta_t} T_t(0, \Delta_t)\mathrm{d}\Delta_t. \tag{15}$$

- The traction–separation curves reach a peak point at a critical crack opening width (δ_{nc}, δ_{tc}),

$$\left.\frac{\partial T_n}{\partial \Delta_n}\right|_{\Delta_n=\delta_{nc}} = 0, \quad \left.\frac{\partial T_t}{\partial \Delta_t}\right|_{\Delta_t=\delta_{tc}} = 0. \tag{16}$$

Notice that the smaller value of the critical crack opening width results in the higher initial slope in the intrinsic traction–separation relationship. The limit of the critical crack opening widths in the PPR potential ($\delta_{nc} \to 0$ and $\delta_{tc} \to 0$) leads to the traction–separation relationship for the extrinsic cohesive zone model.

- The traction value at the critical separation corresponds to the cohesive strength ($\sigma_{\max}$, $\tau_{\max}$),

$$T_n(\delta_{nc}, 0) = \sigma_{\max}, \quad T_t(0, \delta_{tc}) = \tau_{\max}. \tag{17}$$

- The shape parameters (α, β) are introduced in order to represent various material softening responses. When the shape parameters are smaller than two, the cohesive traction–separation relationship illustrates the concave shape (e.g. plateau-type). If $\alpha,\beta \gg 2$, the relation is the convex shape, which can be applicable for typical quasi-brittle materials.

Based on proper boundary conditions, the characteristic parameters (δ_n, δ_t; Γ_n, Γ_t; m, n; α, β) in the PPR potential are determined. The energy constants Γ_n and Γ_t are related to the fracture energies (e.g. modes I and II). When the modes I and II fracture energies are different, one obtains the energy constants

$$\Gamma_n = (-\phi_n)^{\frac{\langle\phi_n-\phi_t\rangle}{\phi_n-\phi_t}}\left(\frac{\alpha}{m}\right)^m, \quad \Gamma_t = (-\phi_t)^{\frac{\langle\phi_t-\phi_n\rangle}{\phi_t-\phi_n}}\left(\frac{\beta}{n}\right)^n \quad \text{for } (\phi_n \neq \phi_t). \tag{18}$$

If the modes I and II fracture energies are the same, the energy constants are simplified as

$$\Gamma_n = -\phi_n\left(\frac{\alpha}{m}\right)^m, \quad \Gamma_t = \left(\frac{\beta}{n}\right)^n \quad \text{for } (\phi_n = \phi_t). \tag{19}$$

The exponents m and n are associated with the initial slope (i.e. artificial compliance),

$$m = \frac{\alpha(\alpha-1)\lambda_n^2}{(1-\alpha\lambda_n^2)}, \quad n = \frac{\beta(\beta-1)\lambda_t^2}{(1-\beta\lambda_t^2)}. \tag{20}$$

where λ_n and λ_t are initial slope indicators, which are the ratio of the critical crack opening width to the final crack opening width, i.e. ($\lambda_n = \delta_{nc}/\delta_n$, $\lambda_t = \delta_{tc}/\delta_t$). The normal final crack opening width (δ_n) is given as

$$\delta_n = \frac{\phi_n}{\sigma_{\max}}\alpha\lambda_n(1-\lambda_n)^{\alpha-1}\left(\frac{\alpha}{m}+1\right)\left(\frac{\alpha}{m}\lambda_n+1\right)^{m-1} \tag{21}$$

while the tangential final crack opening width (δ_t) is expressed as

$$\delta_t = \frac{\phi_t}{\tau_{\max}}\beta\lambda_t(1-\lambda_t)^{\beta-1}\left(\frac{\beta}{n}+1\right)\left(\frac{\beta}{n}\lambda_t+1\right)^{n-1}. \tag{22}$$

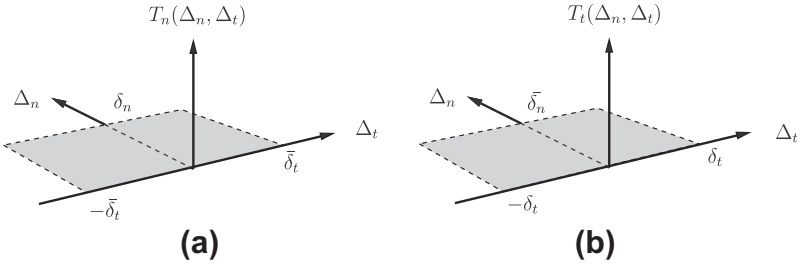

Fig. 2. Description of each cohesive interaction (T_n, T_t) region defined by the final crack opening widths (δ_n, δ_t) and the conjugate final crack opening widths ($\bar{\delta}_n$, $\bar{\delta}_t$).

The cohesive interaction (or softening) region is defined in a rectangular domain, as shown in Fig. 2. The normal cohesive interaction region is determined by the first boundary condition (Eq. (13)), which provides two length scales: the normal final crack opening width (δ_n) and the conjugate tangential final crack opening width ($\bar{\delta}_t$). When normal separation (Δ_n) is greater than δ_n or when the absolute of tangential separation is greater than $\bar{\delta}_t$, the normal cohesive traction is set to be zero. As a result, the normal softening region is a rectangular domain where $0 \leqslant \Delta_n \leqslant \delta_n$ and $|\Delta_t| \leqslant \bar{\delta}_t$. The tangential conjugate final crack opening width ($\Delta_t = \bar{\delta}_t$) is the solution of the following nonlinear function,

$$f_t(\Delta_t) = \Gamma_t \left(1 - \frac{\Delta_t}{\delta_t}\right)^{\beta} \left(\frac{n}{\beta} + \frac{\Delta_t}{\delta_t}\right)^{n} + \langle \phi_t - \phi_n \rangle = 0. \tag{23}$$

The solution ($\bar{\delta}_t$) is unique between 0 and δ_t. Similarly, the second boundary condition (Eq. (14)) defines the tangential cohesive interaction region, i.e. $0 \leqslant \Delta_n \leqslant \bar{\delta}_n$ and $|\Delta_t| \leqslant \delta_t$. The tangential cohesive traction is equal to zero when $\Delta_n \geqslant \bar{\delta}_n$ or $|\Delta_t| \geqslant \delta_t$. The normal conjugate final crack opening width ($\Delta_n = \bar{\delta}_n$) is the solution of the nonlinear function,

$$f_n(\Delta_n) = \Gamma_n \left(1 - \frac{\Delta_n}{\delta_n}\right)^{\alpha} \left(\frac{m}{\alpha} + \frac{\Delta_n}{\delta_n}\right)^{m} + \langle \phi_n - \phi_t \rangle = 0. \tag{24}$$

The solution ($\bar{\delta}_n$) is unique between 0 and δ_n.

The normal cohesive interaction (T_n) is plotted in Fig. 3a with ϕ_n = 100 N/m, ϕ_t = 200 N/m, σ_{max} = 40 MPa, τ_{max} = 30 MPa, α = 5, β = 1.3, λ_n = 0.1, and λ_t = 0.2. When the tangential separation is equal to zero, the normal traction reaches the cohesive strength at $\Delta_n = 0.1\delta_n$, then decreases to zero as Δ_n goes to δ_n, which corresponds to the mode I traction–separation relation-

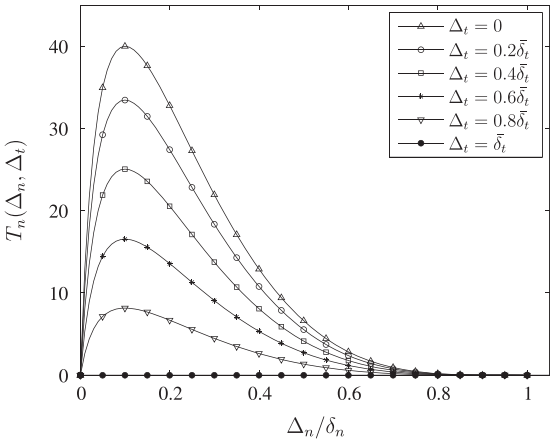

(a)

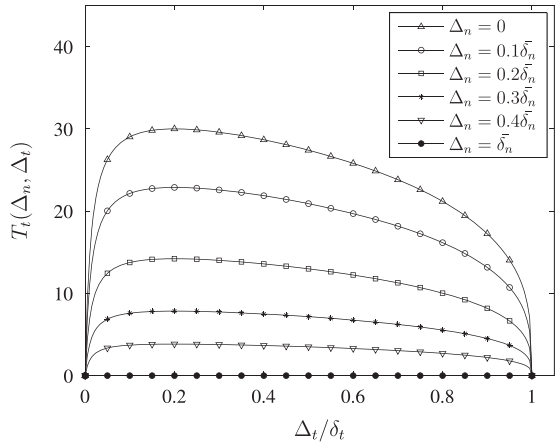

(b)

Fig. 3. (a) Normal cohesive traction with respect to the increase of the tangential separation; (b) tangential cohesive traction with respect to the increase of the normal separation.

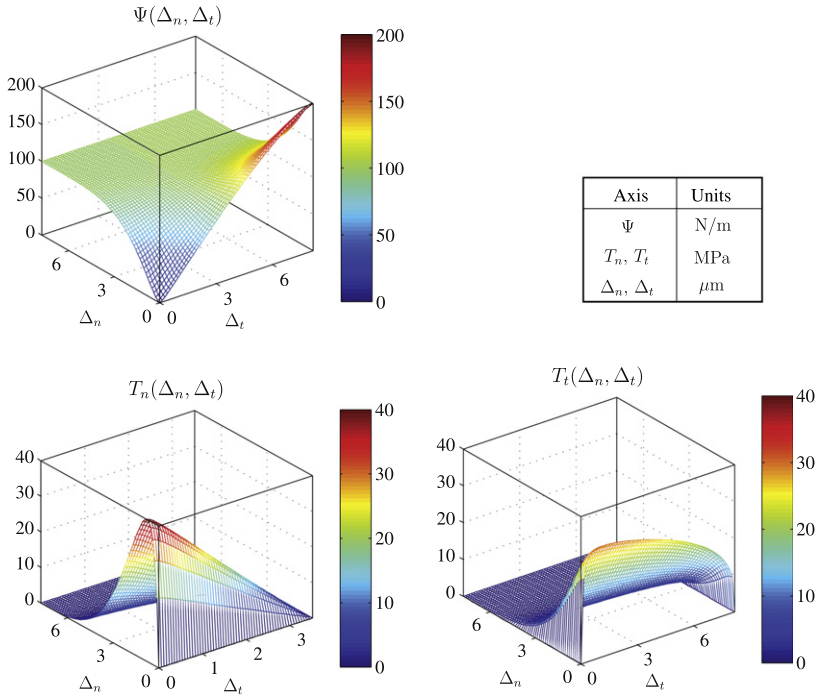

Fig. 4. PPR potential and its gradients for the intrinsic cohesive zone model with ϕ_n = 100 N/m, ϕ_t = 200 N/m, σ_{max} = 40 MPa, τ_{max} = 30 MPa, α = 5, β = 1.3, λ_n = 0.1, and λ_t = 0.2.

ship. The increase of the tangential separation from zero to the conjugate final crack opening width ($\bar{\delta}_t$) leads to the monotonic decrease of the normal cohesive interaction. When Δ_t is equal to $\bar{\delta}_t$, the normal traction is equal to zero, i.e. $T_n(\Delta_n, \bar{\delta}_t) = 0$. Thus, either $\Delta_n \geqslant \delta_n$ or $|\Delta_t| \geqslant \bar{\delta}_t$ results in the complete normal failure condition. Fig. 3b describes the tangential cohesive traction (T_t) with respect to the normal and tangential separations. The tangential traction reaches the peak point when the tangential separation corresponds to the critical separation (i.e. $\Delta_t = 0.2\delta_t$). The tangential traction monotonically decreases with respect to the increase of normal and tangential separations. The tangential traction becomes zero when the tangential separation is greater than or equal to the tangential final crack opening width (δ_t) or when the normal separation is greater than or equal to the normal conjugate final crack opening width ($\bar{\delta}_n$).

The PPR potential and its gradients are plotted in the positive softening region, shown in Fig. 4. The fracture parameters are the same as the parameters used in Fig. 3. The normal cohesive traction illustrates the convex shape while the tangential cohesive traction describes the concave shape, as expected. In addition, the PPR model can be plotted by using a graphical user interface (GUI)[1].

2.3. Unloading/reloading relationship

The dissipation of the fracture energy is associated with unloading and reloading. Thus, unloading/reloading relations are independent of the PPR potential. For simplicity, the following unloading/reloading relationship [1] is provided

$$T_n^{\upsilon}(\Delta_n, \Delta_t) = T_n(\Delta_{n_{max}}, \Delta_t)\left(\frac{\Delta_n}{\Delta_{n_{max}}}\right)^{\alpha_\upsilon}, \quad T_t^{\upsilon}(\Delta_n, \Delta_t) = T_t(\Delta_n, \Delta_{t_{max}})\left(\frac{|\Delta_t|}{\Delta_{t_{max}}}\right)^{\beta_\upsilon}\frac{\Delta_t}{|\Delta_t|}, \tag{25}$$

where $\Delta_{n_{max}}$ is the maximum normal separation in a loading history, while $\Delta_{t_{max}}$ is the maximum absolute of tangential separation in a loading history. The normal and tangential cohesive tractions of the unloading/reloading model are illustrated by black solids in Fig. 5, as an example. Additionally, $T_n(\Delta_{n_{max}}, \Delta_t)$ and $T_t(\Delta_n, \Delta_{t_{max}})$, e.g. gray solids in Fig. 5, correspond to the cohesive tractions along the boundary between the softening condition and the unloading/reloading condition. Unloading/reloading shape parameters (α_υ, β_υ) are introduced to describe various unloading/reloading relations. If α_υ and β_υ are equal to one, the traction–separation relation is linear to the origin. When the shape parameter is smaller than 1, it demonstrates the concave shape. When α_υ, $\beta_\upsilon > 1$, it shows the convex shape.

The unloading/reloading condition is defined on the basis of the normal and tangential separation history. If the current normal separation is greater than $\Delta_{n_{max}}$, the current separation state is normal softening (i.e. follows Eq. (12)). When

[1] A source code written in MATLAB can be found in http://paulino.cee.illinois.edu/education_resources/PPR/GUI.rar

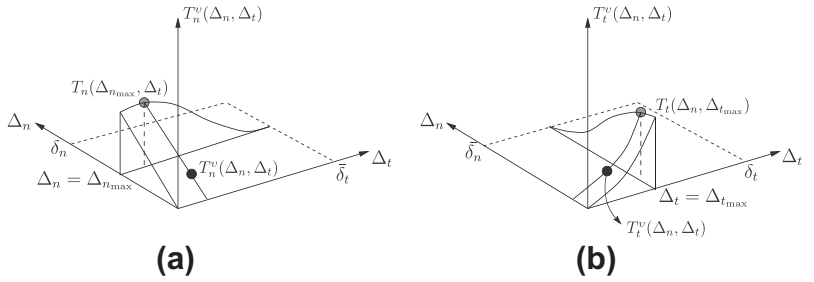

Fig. 5. Schematics of the unloading/reloading model: (a) normal interaction (T_n^v) and (b) tangential interaction (T_t^v).

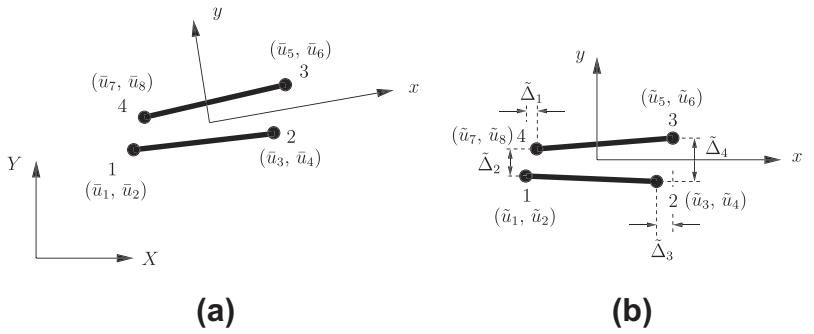

Fig. 6. Two-dimensional linear cohesive element and nodal displacements in (a) the global coordinates and (b) the local coordinates.

$0 < \Delta_n < \Delta_{n_{\max}}$, the current separation state is unloading/reloading, and thus the normal cohesive traction is obtained from the unloading/reloading relationship (i.e. Eq. (25)). Similarly, when the current tangential separation is greater than $\Delta_{t_{\max}}$, the current separation state demonstrates tangential softening. If $|\Delta_t| < \Delta_{t_{\max}}$, the tangential cohesive traction is evaluated on the basis of the unloading/reloading relationship. Then, the unloading/reloading condition for the normal cohesive traction is uncoupled with respect to the unloading/reloading condition for the tangential cohesive traction. Notice that it is possible that the normal cohesive traction demonstrates softening condition while the tangential traction displays unloading/reloading condition. Alternatively, one can employ other unloading/reloading relationships [28,1] in conjunction with the PPR potential.

3. Computational implementation

A finite element-based intrinsic cohesive zone model is implemented as a UEL subroutine in ABAQUS. The subroutine for a two-dimensional linear cohesive element with the PPR potential-based model is provided in Appendix, as an example. In the subroutine, nodal coordinates (`COORDS`), nodal displacements in the global coordinates (`U`), and material parameters defined in an input file (`PROPS`) are available, while the right-hand-side vector (`RHS`) and the Jacobian matrix (`AMATRX`) of a cohesive element need to be defined. In addition, state dependent variables (`SVARS`) can be updated at the end of a nonlinear iteration. In the current implementation, nine input parameters are needed, i.e. normal fracture energy (ϕ_n), tangential fracture energy (ϕ_t), normal cohesive strength ($\sigma_{\max}$), tangential cohesive strength ($\tau_{\max}$), normal shape parameter (α), tangential shape parameter (β), normal initial slope indicator (λ_n), tangential initial slope indicator (λ_t), and thickness of a cohesive element along the out-of-plane direction. The right-hand-side vector (`RHS`) is minus of the internal cohesive force vector, i.e. $-\boldsymbol{f}_{coh}$, while the Jacobian matrix (`AMATRX`) corresponds to the tangent matrix of a cohesive element, i.e. $\boldsymbol{K}_{coh}$. In the state dependent variables (`SVARS`), the maximum normal and tangential separations at each integration point are stored. The two-point Gauss quadrature rule is employed, and thus four state variables are stored at the end of nonlinear iteration. In addition, the unloading/reloading relation is assumed to be linear towards the origin. The two-dimensional linear cohesive element formulation is illustrated in the following subsection. The cohesive traction vector and the tangent matrix are evaluated on the basis of the PPR potential-based model in conjunction with the cohesive interaction region.

3.1. Two-dimensional linear cohesive element

A two-dimensional linear cohesive element consists of four nodes, and each node has two degrees of freedom. Thus, a cohesive element has eight global nodal displacement quantities ($\bar{u}_1, \bar{u}_2, \bar{u}_3, \bar{u}_4, \bar{u}_5, \bar{u}_6, \bar{u}_7, \bar{u}_8$), as shown in Fig. 6a. These global quantities are transformed into local nodal displacement quantities ($\tilde{u}_1, \tilde{u}_2, \tilde{u}_3, \tilde{u}_4, \tilde{u}_5, \tilde{u}_6, \tilde{u}_7, \tilde{u}_8$) by the rotational matrix, $\boldsymbol{R}$

$$\boldsymbol{R} = \begin{bmatrix} \boldsymbol{\Lambda} & \mathbf{0} & \mathbf{0} & \mathbf{0} \\ \mathbf{0} & \boldsymbol{\Lambda} & \mathbf{0} & \mathbf{0} \\ \mathbf{0} & \mathbf{0} & \boldsymbol{\Lambda} & \mathbf{0} \\ \mathbf{0} & \mathbf{0} & \mathbf{0} & \boldsymbol{\Lambda} \end{bmatrix} \tag{26}$$

where the two-dimensional transformation matrix ($\boldsymbol{\Lambda}$) is given as:

$$\boldsymbol{\Lambda} = \begin{bmatrix} \cos\theta & \sin\theta \\ -\sin\theta & \cos\theta \end{bmatrix}. \tag{27}$$

Note that θ is the angle between the global coordinates and the local coordinates. In the current computational implementation, the order of the nodes of a cohesive element is counter clockwise, and the node numbering starts from the lower left node of a cohesive element in the transformed configuration, as shown in Fig. 6b.

Then, the nodal normal separation and tangential separation at the end of a cohesive element ($\widetilde{\Delta}_1$, $\widetilde{\Delta}_2$, $\widetilde{\Delta}_3$, $\widetilde{\Delta}_4$) can be obtained from the local nodal displacement as follows,

$$\widetilde{\Delta}_1 = \tilde{u}_7 - \tilde{u}_1, \quad \widetilde{\Delta}_2 = \tilde{u}_8 - \tilde{u}_2, \quad \widetilde{\Delta}_3 = \tilde{u}_5 - \tilde{u}_3, \quad \widetilde{\Delta}_4 = \tilde{u}_6 - \tilde{u}_4. \tag{28}$$

Based on the above relations, the local displacement–separation relation matrix ($\boldsymbol{L}$) is given as

$$\boldsymbol{L} = \begin{bmatrix} -1 & 0 & 0 & 0 & 0 & 0 & 1 & 0 \\ 0 & -1 & 0 & 0 & 0 & 0 & 0 & 1 \\ 0 & 0 & -1 & 0 & 1 & 0 & 0 & 0 \\ 0 & 0 & 0 & -1 & 0 & 1 & 0 & 0 \end{bmatrix}. \tag{29}$$

The separation along the cohesive element is obtained from the nodal separation quantities in conjunction with the shape functional matrix ($\boldsymbol{N}$),

$$\boldsymbol{N} = \begin{bmatrix} N_1 & 0 & N_2 & 0 \\ 0 & N_1 & 0 & N_2 \end{bmatrix} \tag{30}$$

where the linear shape functions in the natural coordinate (ξ) are given as

$$N_1 = \frac{1-\xi}{2}, \quad N_2 = \frac{1+\xi}{2}. \tag{31}$$

From Eqs. (26)–(30), the global displacement–separation relation matrix ($\boldsymbol{B}_c$) is expressed as

$$\boldsymbol{B}_c = \begin{bmatrix} -CN_1 & -SN_1 & -CN_2 & -SN_2 & CN_2 & SN_2 & CN_1 & SN_1 \\ SN_1 & -CN_1 & SN_2 & -CN_2 & -SN_2 & CN_2 & -SN_1 & CN_1 \end{bmatrix} \tag{32}$$

where C and S denote $\cos\theta$ and $\sin\theta$, respectively. Finally, the internal cohesive force vector (Eq. (8)) and the tangent matrix (Eq. (9)) are computed by using a numerical integration scheme (e.g. Gauss quadrature).

3.2. Determination of cohesive interaction region

The cohesive interaction (softening) region is associated with the length scales: the final crack opening widths (δ_n, δ_t) and the conjugate final crack opening widths ($\bar{\delta}_n$, $\bar{\delta}_t$). The softening region of the normal cohesive traction is defined as $0 \leqslant \Delta_n \leqslant \delta_n$ and $-\bar{\delta}_t \leqslant \Delta_t \leqslant \bar{\delta}_t$ while the softening region of the tangential cohesive traction is defined as $0 \leqslant \Delta_n \leqslant \bar{\delta}_n$ and $-\delta_t \leqslant \Delta_t \leqslant \delta_t$. For the intrinsic cohesive zone model, the normal and tangential final crack opening widths are determined by the closed form (Eqs. (21) and (22)), while the conjugate final crack opening widths are calculated by solving the nonlinear equations (Eqs. (23) and (24)). The nonlinear equations can be solved by a root-finding algorithm, such as the Bisection method or the Newton–Raphson method.

Alternatively, the softening region can be defined without solving the nonlinear equation. The necessary and sufficient conditions of $(-\bar{\delta}_t \leqslant \Delta_t \leqslant \bar{\delta}_t)$, associated with the normal softening region, are $((-\delta_t \leqslant \Delta_t \leqslant \delta_t)\ \&\ (T_n(\Delta_n, \Delta_t) \geqslant 0))$. This is because the tangential conjugate final crack opening width $(\bar{\delta}_t)$ is unique between zero and the tangential final crack opening width (δ_t) and because the normal cohesive traction is always positive within the normal softening region. Similarly, one can replace $(0 \leqslant \Delta_n \leqslant \bar{\delta}_n)$ by $((0 \leqslant \Delta_n \leqslant \delta_n)\ \&\ (T_t(\Delta_n, \Delta_t) \geqslant 0))$ because $\bar{\delta}_n$ is unique between 0 and δ_n, and because the tangential traction is positive within the tangential softening region. Notice that this alternative approach is employed in the UEL subroutine provided in Appendix.

3.3. Cohesive traction vector and tangent matrix

The cohesive traction vector and the material tangent stiffness matrix are evaluated by accounting for four cases: softening, unloading/reloading, contact and complete failure conditions. Algorithm 1 outlines the evaluation of the cohesive traction vector ($\boldsymbol{T}_c$) and tangent matrix ($\boldsymbol{D}_c$) with respect to the four cases. Notice that the normal and tangential cohesive interactions are evaluated independently.

Algorithm 1. Evaluation of the cohesive traction vector and tangent matrix based on the four conditions: softening, unloading/reloading, contact and complete failure.

// **Normal cohesive interaction:**
if $(\Delta_n \leqslant 0)$ **then** {*Contact*}
$T_n = D_{nn}\Delta_n, \quad D_{nn} = \alpha_p, \quad D_{nt} = 0$
else if $(0 \leqslant \Delta_n \leqslant \delta_n \quad \text{and} \quad |\Delta_t| \leqslant \bar{\delta}_t \quad \text{and} \quad \Delta_n \geqslant \Delta_{n_{\max}})$ **then** {*Softening*}
$T_n = \frac{\partial \Psi(\Delta_n,\Delta_t)}{\partial \Delta_n}, \quad D_{nt} = \frac{\partial^2 \Psi(\Delta_n,\Delta_t)}{\partial \Delta_n^2}, \quad D_{nt} = \frac{\partial^2 \Psi(\Delta_n,\Delta_t)}{\partial \Delta_n \partial \Delta_t}$
else if $(0 \leqslant \Delta_n \leqslant \delta_n \quad \text{and} \quad |\Delta_t| \leqslant \bar{\delta}_t \quad \text{and} \quad \Delta_n < \Delta_{n_{\max}})$ **then** {*Unloading/reloading*}
$T_n = T_n^v(\Delta_n, \Delta_t), \quad D_{nn} = \frac{\partial T_n^v(\Delta_n,\Delta_t)}{\partial \Delta_n}, \quad D_{nt} = \frac{\partial T_n^v(\Delta_n,\Delta_t)}{\partial \Delta_t}$
else if $(\Delta_n > \delta_n \quad \text{or} \quad |\Delta_t| > \bar{\delta}_t)$ **then** {*Complete failure*}
$T_n = 0, \quad D_{nn} = 0, \quad D_{nt} = 0$
end if

// **Tangential cohesive interaction:**
if $(\Delta_n \leqslant 0)$ **then** {*Contact*}
$\Delta_n = 0$
end if

if $(0 \leqslant \Delta_n \leqslant \bar{\delta}_n \quad \text{and} \quad |\Delta_t| \leqslant \delta_t \quad \text{and} \quad |\Delta_t| \geqslant \Delta_{t_{\max}})$ **then** {*Softening*}
$T_t = \frac{\partial \Psi(\Delta_n,\Delta_t)}{\partial \Delta_t}, \quad D_{tn} = \frac{\partial^2 \Psi(\Delta_n,\Delta_t)}{\partial \Delta_t \Delta_n}, \quad D_{tt} = \frac{\partial^2 \Psi(\Delta_n,\Delta_t)}{\partial \Delta_t^2}$
else if $(0 \leqslant \Delta_n \leqslant \bar{\delta}_n \quad \text{and} \quad |\Delta_t| \leqslant \delta_t \quad \text{and} \quad |\Delta_t| < \Delta_{t_{\max}})$ **then** {*Unloading/reloading*}
$T_t = T_t^v(\Delta_n, \Delta_t), \quad D_{tn} = \frac{\partial T_t^v(\Delta_n,\Delta_t)}{\partial \Delta_n}, \quad D_{tt} = \frac{\partial T_t^v(\Delta_n,\Delta_t)}{\partial \Delta_t}$
else if $((\Delta_n > \bar{\delta}_n) \quad \text{or} \quad (|\Delta_t| > \delta_t))$ **then** {*Complete failure*}
$T_t = 0, \quad D_{tn} = 0, \quad D_{tt} = 0$
end if

First, when separations are within the cohesive interaction region and when the current separation is greater than the maximum separation in a loading history, the current state of separation follows the *softening condition*. Thus, the constitutive relationship is derived from the PPR potential. If both normal and tangential separations are in the softening condition, the cohesive tractions are evaluated by taking the derivatives of the PPR potential,

$$\boldsymbol{T}_c(\Delta_n, \Delta_t) = \left\{ \begin{array}{l} \partial \Psi / \partial \Delta_t \\ \partial \Psi / \partial \Delta_n \end{array} \right\} = \left\{ \begin{array}{l} T_t(\Delta_n, \Delta_t) \\ T_n(\Delta_n, \Delta_t) \end{array} \right\}, \tag{33}$$

as shown in Eq. (12). The second derivatives of the PPR potential lead to the material tangent stiffness matrix,

$$\boldsymbol{D}_c(\Delta_n, \Delta_t) = \begin{bmatrix} D_{tt} & D_{tn} \\ D_{nt} & D_{nn} \end{bmatrix} = \begin{bmatrix} \partial^2 \Psi / \partial \Delta_t^2 & \partial^2 \Psi / \partial \Delta_t \partial \Delta_n \\ \partial^2 \Psi / \partial \Delta_n \partial \Delta_t & \partial^2 \Psi / \partial \Delta_n^2 \end{bmatrix}, \tag{34}$$

where the components of the matrix are given as

$$\begin{aligned}
D_{nn} &= \frac{\Gamma_n}{\delta_n^2}\left[(m^2-m)\left(1-\frac{\Delta_n}{\delta_n}\right)^{\alpha}\left(\frac{m}{\alpha}+\frac{\Delta_n}{\delta_n}\right)^{m-2} + (\alpha^2-\alpha)\left(1-\frac{\Delta_n}{\delta_n}\right)^{\alpha-2}\left(\frac{m}{\alpha}+\frac{\Delta_n}{\delta_n}\right)^{m}\right. \\
&\quad \left. -2\alpha m\left(1-\frac{\Delta_n}{\delta_n}\right)^{\alpha-1}\left(\frac{m}{\alpha}+\frac{\Delta_n}{\delta_n}\right)^{m-1}\right]\left[\Gamma_t\left(1-\frac{|\Delta_t|}{\delta_t}\right)^{\beta}\left(\frac{n}{\beta}+\frac{|\Delta_t|}{\delta_t}\right)^{n} + \langle \phi_t - \phi_n \rangle\right], \\
D_{nt} &= \frac{\Gamma_n \Gamma_t}{\delta_n \delta_t}\left[m\left(1-\frac{\Delta_n}{\delta_n}\right)^{\alpha}\left(\frac{m}{\alpha}+\frac{\Delta_n}{\delta_n}\right)^{m-1} - \alpha\left(1-\frac{\Delta_n}{\delta_n}\right)^{\alpha-1}\left(\frac{m}{\alpha}+\frac{\Delta_n}{\delta_n}\right)^{m}\right] \\
&\quad \left[n\left(1-\frac{|\Delta_t|}{\delta_t}\right)^{\beta}\left(\frac{n}{\beta}+\frac{|\Delta_t|}{\delta_t}\right)^{n-1} - \beta\left(1-\frac{|\Delta_t|}{\delta_t}\right)^{\beta-1}\left(\frac{n}{\beta}+\frac{|\Delta_t|}{\delta_t}\right)^{n}\right]\frac{\Delta_t}{|\Delta_t|}, \\
D_{tn} &= D_{nt}, \\
D_{tt} &= \frac{\Gamma_t}{\delta_t^2}\left[(n^2-n)\left(1-\frac{|\Delta_t|}{\delta_t}\right)^{\beta}\left(\frac{n}{\beta}+\frac{|\Delta_t|}{\delta_t}\right)^{n-2} + (\beta^2-\beta)\left(1-\frac{|\Delta_t|}{\delta_t}\right)^{\beta-2}\left(\frac{n}{\beta}+\frac{|\Delta_t|}{\delta_t}\right)^{n}\right. \\
&\quad \left. -2\beta n\left(1-\frac{|\Delta_t|}{\delta_t}\right)^{\beta-1}\left(\frac{n}{\beta}+\frac{|\Delta_t|}{\delta_t}\right)^{n-1}\right]\left[\Gamma_n\left(1-\frac{\Delta_n}{\delta_n}\right)^{\alpha}\left(\frac{m}{\alpha}+\frac{\Delta_n}{\delta_n}\right)^{m} + \langle \phi_n - \phi_t \rangle\right].
\end{aligned} \tag{35}$$

In this case, as expected, one obtains the symmetric tangent stiffness matrix.

Next, when separations are within the cohesive interaction region and when the current separation is smaller than the maximum separation, the current state corresponds to the *unloading/reloading condition*. Then, the cohesive traction is obtained from the unloading/reloading model (Eq. (25)), and its Jacobian matrix is given by

$$\boldsymbol{D}_c(\Delta_n, \Delta_t) = \begin{bmatrix} D_{tt}^{\upsilon} & D_{tn}^{\upsilon} \\ D_{nt}^{\upsilon} & D_{nn}^{\upsilon} \end{bmatrix} = \begin{bmatrix} \partial T_t^{\upsilon}/\partial \Delta_t & \partial T_t^{\upsilon}/\partial \Delta_n \\ \partial T_n^{\upsilon}/\partial \Delta_t & \partial T_n^{\upsilon}/\partial \Delta_n \end{bmatrix} \tag{36}$$

where the entries are expressed as

$$\begin{aligned} D_{nn}^{\upsilon} &= T_n(\Delta_{n_{\max}}, \Delta_t)\frac{\alpha_{\upsilon}}{\Delta_{n_{\max}}}\left(\frac{\Delta_n}{\Delta_{n_{\max}}}\right)^{\alpha_{\upsilon}-1} \\ D_{nt}^{\upsilon} &= D_{nt}(\Delta_{n_{\max}}, \Delta_t)\left(\frac{\Delta_n}{\Delta_{n_{\max}}}\right)^{\alpha_{\upsilon}} \\ D_{tn}^{\upsilon} &= D_{tn}(\Delta_n, \Delta_{t_{\max}})\left(\frac{|\Delta_t|}{\Delta_{t_{\max}}}\right)^{\beta_{\upsilon}} \\ D_{tt}^{\upsilon} &= T_t(\Delta_n, \Delta_{t_{\max}})\frac{\beta_{\upsilon}}{\Delta_{t_{\max}}}\left(\frac{|\Delta_t|}{\Delta_{t_{\max}}}\right)^{\beta_{\upsilon}-1}. \end{aligned} \tag{37}$$

In this case, the symmetric system is not guaranteed because the unloading/reloading model is not derived from a potential.

The *contact condition* occurs when the normal separation is negative. In this case, the normal negative separation can be penalized to prevent from material self-penetration. For example, the normal cohesive interaction is calibrated using the penalty stiffness (α_p), i.e. $T_n = \alpha_p \Delta_n$. In this study, α_p is selected as the stiffness at the zero separation, i.e.

$$\alpha_p = \left.\frac{\partial^2 \Psi(\Delta_n, \Delta_t)}{\partial \Delta_n^2}\right|_{\Delta_n=0,\ \Delta_t=0}. \tag{38}$$

The tangential cohesive interaction is evaluated by penalizing $\Delta_n = 0$ (see Algorithm 1). Alternative approaches, involving contact mechanics, may also be applicable.

Finally, material locally experiences *complete failure* when separations are outside of the cohesive interaction region. The normal cohesive traction and normal stiffness matrix entries are set to be zero either when normal separation is greater than the normal final crack opening width ($\Delta_n > \delta_n$), or when the absolute value of tangential separation is greater than the tangential conjugate final crack opening width ($|\Delta_t| > \bar{\delta}_t$). Notice that the normal cohesive interaction is continuous (i.e. no truncation) along the boundary of the normal interaction region (i.e. $\Delta_n = \delta_n$ and $|\Delta_t| = \bar{\delta}_t$), because the normal cohesive interaction satisfies the boundary conditions of ($T_n(\delta_n, \Delta_t) = 0$ and $T_n(\Delta_n, \bar{\delta}_t) = 0$). Similarly, the tangential cohesive interaction and tangential stiffness matrix entries are equal to zero when either $\Delta_n > \bar{\delta}_n$ or $|\Delta_t| > \delta_t$. The tangential cohesive interaction is continuous along the boundary of the tangential softening region (i.e. $\Delta_n = \bar{\delta}_n$ and $|\Delta_t| = \delta_t$), because the tangential cohesive interaction satisfies the boundary conditions of ($T_t(\bar{\delta}_n, \Delta_t) = 0$ and $T_t(\Delta_n, \delta_t) = 0$).

4. Examples

For the intrinsic cohesive zone modeling approach, cohesive surface elements are inserted in a potential crack propagation region before computational simulation. Then, cohesive elements and their material properties are defined in an ABAQUS input file to simulate example problems. For instance, cohesive elements are declared by means of `*USER ELEMENT` command, e.g.

```
*USER ELEMENT, TYPE = U1, NODES = 4, COORDINATES = 2, PROPERTIES = 9, VARIABLES = 4
1, 2
```

Note that `TYPE` indicates the name of the element type (e.g. `U1`), `NODES` is the number of nodes, `COORDINATES` is the largest active degree of freedom, `PROPERTIES` is the number of the input parameters (`PROPS`), and `VARIABLES` is the number of the solution dependent variables (`SVARS`). Then, active degrees of freedom are listed below, i.e. `1, 2`, which corresponds to horizontal and vertical displacements. For the given element type (e.g. `U1`), element connectivities are provided as follows:

```
*ELEMENT, TYPE = U1, ELSET = COH_ELE
101, 1, 2, 3, 4
```

where `ELSET` is the name of element set (e.g. `COH_ELE`) to which these elements will be assigned. For the given element set (e.g. `COH_ELE`), the input parameters (`PROPS`) are defined as follows:

```
*UEL PROPERTY, ELSET = COH_ELE
100, 200, 4e6, 3e6, 5, 1.6, 0.005, 0.005,
0.01
```

where input parameters are provided as an example. Nine parameters are required, and listed as the following orders: ϕ_n, ϕ_t, σ_{max}, τ_{max}, α, β, λ_n, λ_t, and thickness along the out-of-plane direction. After generating an input file, one can execute an analysis in conjunction with the UEL subroutine through the following command, i.e.

```
abaqus job = input_file_name user = UEL_file_name
```

More detailed information associated with an ABAQUS input file and its execution can be found in the ABAQUS/standard user's manual [16].

In order to verify the UEL subroutine, three computational examples are provided: patch test, mixed-mode bending test, and matrix/particle debonding. For patch tests, simple mode-I and mode-II tests are simulated, which display constant stress state within continuum (or bulk) elements. In addition, mixed-mode bending and matrix/particle debonding examples are investigated by comparing computational results to analytical solutions.

4.1. Patch test: mode-I and mode-II

In order to verify computational implementation, simple modes I and II problems are first introduced. The geometry of modes I and II problems is described in Fig. 7. The elastic modulus is 32 GPa, and the Poisson's ratio is 0.2. The fracture parameters of the PPR model are given as $\phi_n = 100$ N/m, $\phi_t = 200$ N/m, $\sigma_{max} = 4$ MPa, $\tau_{max} = 3$ MPa, $\alpha = 5$, $\beta = 1.6$,$\lambda_n = 0.005$, and $\lambda_t = 0.005$. The unloading/reloading relation is assumed to be linear to the origin, as indicated previously.

For a mode I test, a square plate (0.1 m $\times$ 0.1 m) is elongated at the top under the displacement control up to 0.03 mm. Next, the plate is compressed until the displacement at the top is -0.01 mm, and is elongated again to demonstrate complete failure condition. The plate is discretized by a bilinear quadrilateral element (Q4), and a cohesive element is inserted at the bottom of the plate (see Fig. 7a). The stress versus displacement relation is plotted in Fig. 8a. While the plate is elongated, stress initially increases up to the cohesive strength (σ_{max}), and then the plate demonstrates softening behavior. The softening curve is convex because the mode I shape parameter is greater than 2 (i.e. $\alpha = 5$). When the plate is unloaded, the cohesive traction is evaluated on the basis of the linear unloading/reloading relationship.

For a mode II problem, a 0.1 m by 0.1 m plate is elongated and compressed at the top and right hand sides up to 0.04 mm. Then, the displacements are applied along the opposite directions up to -0.05 mm, and are reversed again until the complete failure. In this case, the principal stresses are along the horizontal and vertical directions, and the maximum shear stress occurs along the 45°. The magnitude of the maximum shear stress is equal to the magnitude of the principal stresses. The plate is discretized by two linear triangular elements (T3), and a cohesive element is inserted along the diagonal direction (see Fig. 7b). Fig. 8b illustrates that the maximum shear stress reaches the cohesive strength, and the softening curve is concave because the mode II shape parameter (β) less than two. Then, the plate is linearly unloaded and reloaded, while the applied displacement changes from 0.04 mm to -0.04 mm, and from 0.05 mm to -0.05 mm. Finally, the increase of the applied displacement leads to softening and complete failure conditions.

4.2. Mixed-mode bending analysis

Mixed-mode bending tests are employed to estimate the fracture energy under mixed mode conditions [29]. Note that the problem is considered in Ref [15]. The geometry of the test is shown in Fig. 9. For the test configuration, the analytical solution is available, which consists of three parts based on the linear beam theory (one part) and linear elastic fracture mechanics (two parts) [30]. The domain is discretized with bilinear quadrilateral elements (Q4), and cohesive elements are inserted along the horizontal direction, which corresponds to the potential crack path, i.e. the intrinsic cohesive zone model. The number of bilinear quadrilateral elements is 19,570 while the number of cohesive elements is 683. The material properties are arbitrarily selected. The elastic modulus and the Poisson's ratio are 122 GPa and 0.25, respectively. Force boundary conditions are applied where a rigid lever is located, while displacement boundary conditions are employed where the beam is supported. Additionally, a modified Riks method [31,16] is utilized to capture post-peak load behavior.

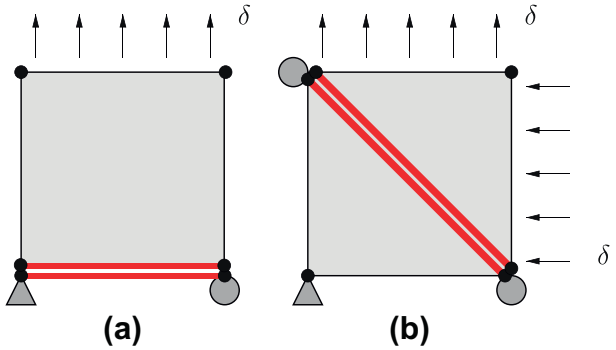

Fig. 7. Geometry of (a) mode I test, and (b) mode II test.

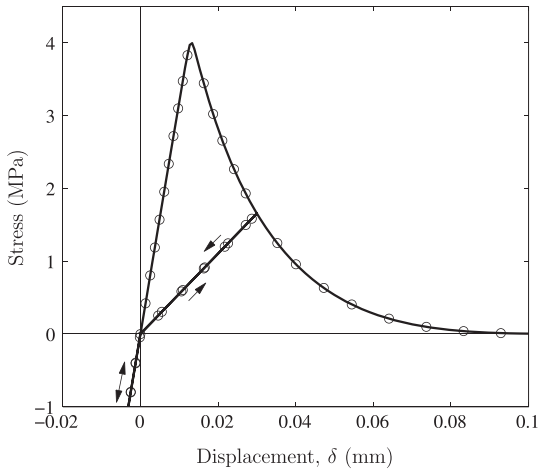

Fig. 8. Computational results: (a) mode I test, and (b) mode II test.

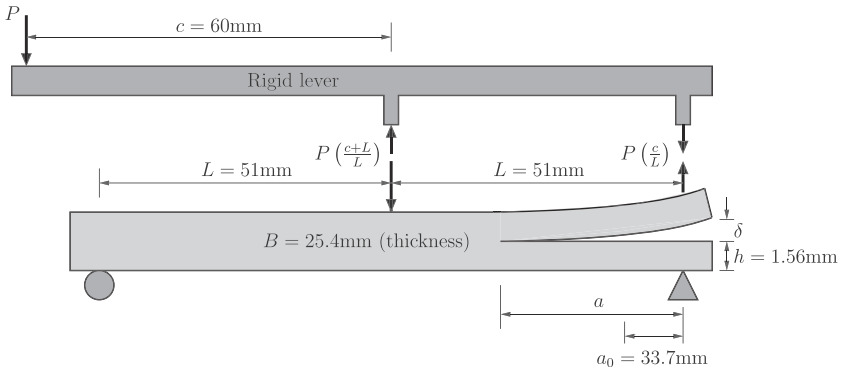

Fig. 9. Geometry of the mixed-mode bending test.

In this study, two cases are tested. One is that the mode I fracture energy is the same as the mode II fracture energy (e.g. $\phi_n = \phi_t = 500$ N/m). The other is that the mode I fracture energy is different from the mode II fracture energy (e.g. $\phi_n = 500$ N/m, $\phi_t = 1000$ N/m). The shape parameter (α,β) is 3, and the initial slope indicator (λ_n,λ_t) is 0.02 for both cases. For the same fracture energy, the computational results obtained with various cohesive strengths (σ_{max}, τ_{max}) are illustrated in Fig. 10a. The increase

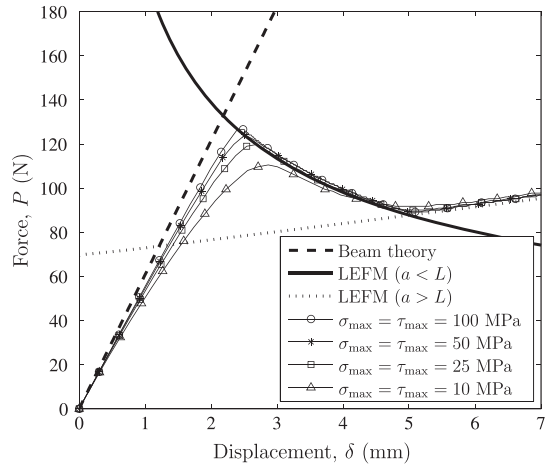

(a)

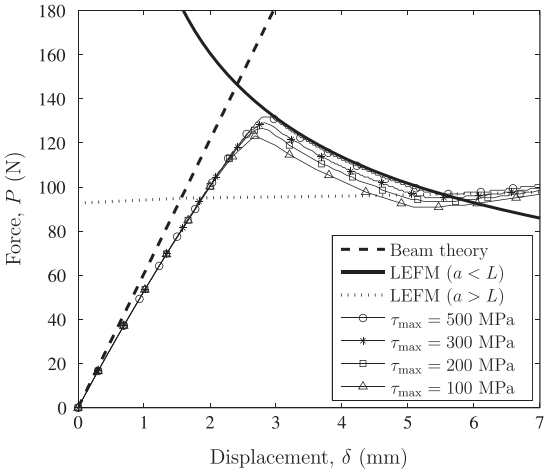

(b)

Fig. 10. Comparison between the analytical solutions and the computational results: (a) $\phi_n = \phi_t = 500$ N/m, and (b) $\phi_n = 500$ N/m, $\phi_t = 1000$ N/m.

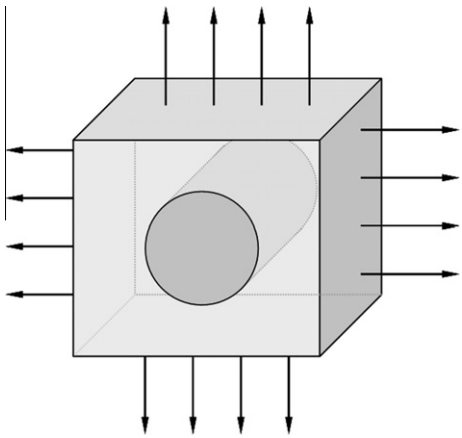

Fig. 11. Unit cell with a cylindrical particle under equi-biaxial tension stress state.

of the cohesive strength leads to more brittle failure behavior, and thus demonstrates the convergence to the analytical solutions. For the case of different fracture energies, the normal cohesive strength is fixed as 20 MPa while the tangential cohesive strength changes from 100 MPa to 500 MPa. Similarly, the computational results converges to the analytical solutions while the tangential cohesive strength (τ_{max}) increases, as shown in Fig. 10b.

4.3. Multiscale analysis through matrix/particle debonding

Matrix/particle debonding process is analyzed, and computational results are compared with the results obtained from a micro-mechanics approach. In this study, one assumes that all particles are isotropic, and have the same elastic modulus and particle size. The shape of a unit cell are a regular hexahedron with a cylindrical particle, as illustrated in Fig. 11. Boundary conditions of a unit cell are idealized as the equibiaxial tension under plane strain condition. The particle volume fraction (f) is associated with the unit cell size and the radius of particle (a_p). Based on the extended Mori–Tanaka method [32,13], the macroscopic strain ($\bar{\epsilon}$) and the macroscopic stress ($\bar{\sigma}$) are given as:

$$\bar{\epsilon} = \frac{(1+\nu^m)(1-2\nu^m)}{E^m}\bar{\sigma} + f\left\{\left(\frac{(1+\nu^p)(1-2\nu^p)}{E^p} - \frac{(1+\nu^m)(1-2\nu^m)}{E^m}\right)\bar{\sigma}^p + \frac{\Delta_n}{a_p}\right\} \tag{39}$$

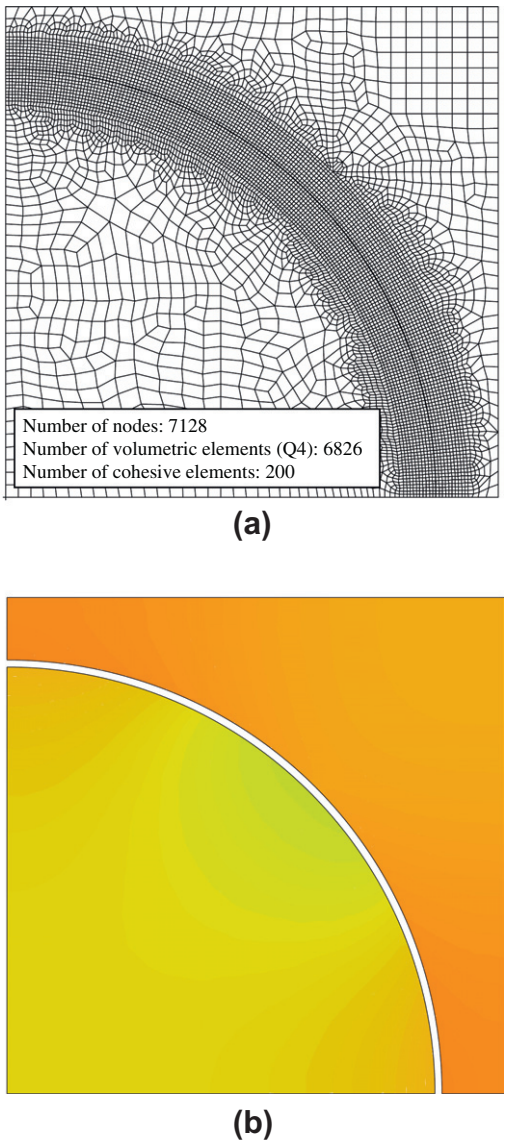

Fig. 12. (a) Finite element mesh of the unit cell, and (b) Mises stress distribution for the case of σ_{max} = 10 MPa.

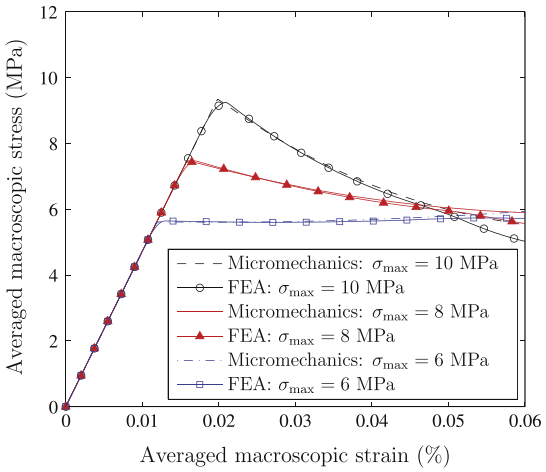

Fig. 13. Macroscopic stress versus strain relations with respect to the change of the cohesive strength.

and

$$\bar{\sigma} = \frac{(1-f)E^m}{2(1-\nu^m)(1+\nu^m)}\left\{\left(\frac{(1+\nu^p)(1-2\nu^p)}{E^p}+\frac{1+\nu^m}{E^m}\right)\bar{\sigma}^p+\frac{\Delta_n}{a_p}\right\}+f\bar{\sigma}^p, \tag{40}$$

where E^m and E^p are elastic modulus of matrix and particle, and ν^m and ν^p are Poisson's ratio of matrix and particle, respectively. In addition, the average stress in the particle ($\bar{\sigma}^p$) is uniform, and thus equals to the normal cohesive traction at the particle/matrix interface (T_n), which is related to the normal separation (Δ_n) in the PPR model.

The particle size (a_p) is 2 cm, and the volume fraction (f) of the particle is 0.6. A quarter of the unit cell is analyzed because of symmetry along the horizontal and vertical directions. The corresponding finite element mesh is illustrated in Fig. 12a, and cohesive elements are inserted along the matrix/particle interface. The elastic modulus of particle (E^p) is 40 GPa while the modulus of matrix (E^m) is 20 GPa. Both particle and matrix have the same Poisson's ratio, i.e. $\nu^p = \nu^m = 0.25$. The mode I fracture parameters are assumed to be the same as the mode II fracture parameters. The fracture energy is 100 N/m, the shape parameter is 3, and the initial slope indicator is 0.001. Three cases are tested by changing the cohesive strength, i.e. σ_{max} = 10 MPa, 8 MPa and 6 MPa. Fig. 12b illustrates the stress distribution after the peak load for the case of σ_{max} = 10 MPa. In addition, the macroscopic stress versus strain relations obtained from the finite element computation are compared with the results from the extended Mori–Tanaka method, as shown in Fig. 13. The increase of the cohesive strength leads to more brittle failure behavior, and increases the peak stress of the averaged macroscopic stress.

5. Concluding remarks

This paper presents the implementation of the PPR potential-based model in ABAQUS using a UEL subroutine. The implementation is based on the intrinsic cohesive zone modeling approach, which includes the initial elastic range in the traction–separation relation. The input file format is provided for educational purposes. The UEL subroutine is provided in Appendix. In the PPR potential-based model, the cohesive traction and its tangent matrix are evaluated by considering four conditions: softening, unloading/reloading, contact and complete failure. The cohesive traction is obtained from the PPR potential for the softening condition, while it is computed from the unloading/reloading model for the unloading/reloading condition. For the contact condition, a penalty stiffness is introduced along the normal direction to prevent material interpenetration. The complete failure condition is associated with the cohesive interaction region. The interaction region is defined within the final crack opening width (δ_n, δ_t) and the conjugate final crack opening width ($\bar{\delta}_n$, $\bar{\delta}_t$) space. Note that δ_n and δ_t are explicitly computed, while $\bar{\delta}_n$ and $\bar{\delta}_t$ can be computed by solving a nonlinear equation. Alternatively, rather than solving a nonlinear equation, the interaction region can be determined by checking the sign of the cohesive traction. Finally, three computational examples are investigated to verify the present formulation: patch test, mixed-mode bending test, and matrix/particle debonding. We have shown how to implement the PPR model in ABAQUS/Standard, which includes an implicit solution technique. We close this paper with a challenge for students interested in this line of research. We suggest that those students implement the PPR model in ABAQUS/Explicit and explore simulations of cohesive elasto-dynamic fracture such as those presented in reference [33].

Acknowledgements

Dr. Park acknowledges support from the National Research Foundation (NRF) of Korea through Grant Young Researchers #2011-0013393. The information presented in this paper is the sole opinion of the authors and does not necessarily reflect the views of the sponsoring agency.

Appendix A[2]

```
c ======================================================================
c Two-Dimensional Linear Cohesive Zone Element for the Intrinsic Model
c Developed by Kyoungsoo Park and Glaucio H. Paulino
c
c Kyoungsoo Park
c School of Civil and Environmental Engineering
c Yonsei University, Seoul, S. Korea
c
c Glaucio H. Paulino
c Department of Civil and Environmental Engineering
c University of Illinois at Urbana-Champaign, U.S.A.
c
c References
c
c K. Park, and G.H. Paulino, 2012, Implementation of the PPR potential-
c   based model in ABAQUS: Educational perspective, Engineering Fracture
c   Mechanics 93,239-262
c   DOI: http://dx.doi.org/10.1016/j.engfracmech.2012.02.007
c K. Park, G.H. Paulino, and J.R. Roesler, 2009, A unified potential-based
c   cohesive model of mixed-mode fracture, Journal of the Mechanics and
c   Physics of Solids 57 (6), 891-908.
c   DOI: http://dx.doi.org/10.1016/j.jmps.2008.10.003
c K. Park, 2009, Potential-based fracture mechanics using cohesive zone
c   and virtual internal bond modeling, PhD Thesis, University of
c   Illinois at Urbana-Champaign.
c
c SUBROUTINE UEL
c  : Main function for the computational implementation of
c    a two-dimensional linear intrinsic cohesive element
c SUBROUTINE k_Cohesive_PPR
c  : Function to compute the traction-separation relationship
c    of the PPR potential-based model
c SUBROUTINE k_Coords_Transform
c  : Function to compute the coordinate transformation matrix
c    between the global and local coordinates
c SUBROUTINE k_Matrix_Zero      : Matrix operation (A = 0)
c SUBROUTINE k_Matrix_Transpose  : Matrix operation (B = A_t)
c SUBROUTINE k_Matrix_PlusScalar : Matrix operation (A = A + c * B)
c SUBROUTINE k_Matrix_Multiply   : Matrix operation (C = A * B)
c
c ======================================================================
      SUBROUTINE UEL (RHS, AMATRX, SVARS, ENERGY, NDOFEL, NRHS, NSVARS,
     & PROPS, NPROPS, COORDS, MCRD, NNODE, U, DU, V, A, JTYPE, TIME,
     & DTIME, KSTEP, KINC, JELEM, PARAMS, NDLOAD, JDLTYP, ADLMAG,
     & PREDEF, NPREDF, LFLAGS, MLVARX, DDLMAG, MDLOAD, PNEWDT, JPROPS,
     & NJPRO, PERIOD)
      INCLUDE 'ABA_PARAM.INC'
      DIMENSION RHS(MLVARX,*), AMATRX(NDOFEL,NDOFEL), PROPS(*),
     & SVARS(*), ENERGY(8), COORDS(MCRD, NNODE), U(NDOFEL),
     & DU(MLVARX,*), V(NDOFEL), A(NDOFEL), TIME(2), PARAMS(*),
     & JDLTYP(MDLOAD,*), ADLMAG(MDLOAD,*), DDLMAG(MDLOAD,*),
     & PREDEF(2, NPREDF, NNODE), LFLAGS(*), JPROPS(*)
c Variables defined in the UEL subroutine
c   RHS   : Right-Hand-Side vector
c   AMATRX: Stiffness (Jacobian) matrix
c
c Variables updated in the UEL subroutine
c   SVARS : Maximum separation at each integration point
c
c Variables available in the UEL subroutine
```

[2] The source code provided in this appendix can be downloaded from the urlhttp://paulino.cee.illinois.edu or http://k-park.yonsei.ac.kr

```
c   U    : Nodal displacement
c   COORDS: Nodal coordinates of an element
c   PROPS : Parameters from an input file
c      PROPS(1): Normal fracture energy (Gn)
c      PROPS(2): Tangential fracture energy (Gt)
c      PROPS(3): Normal cohesive strength (Tn_m)
c      PROPS(4): Tangential cohesive strength (Tt_m)
c      PROPS(5): Normal shape parameter (alph)
c      PROPS(6): Tangential shape parameter (beta)
c      PROPS(7): Normal initial slope indicator (ln)
c      PROPS(8): Tangential initial slope indicator (lt)
c      PROPS(9): Thickness of a cohesive element
c   MCRD  : Largest active degrees of freedom
c   NNODE : Number of nodes
c
c Variables used in the UEL subroutine
      DIMENSION Sc(ndofel,ndofel), Fc(ndofel,nrhs),
     & T(mcrd,nrhs), T_d(mcrd,mcrd), U_l(ndofel), R(mcrd, mcrd),
     & Bc(mcrd,ndofel), Bct(ndofel,mcrd), ShapeN(nnode),
     & del(mcrd), GP(2), GP_w(2), tmp(ndofel,mcrd)
c   Sc  : Element stiffness matrix of a cohesive element
c   Fc  : Cohesive internal force vector
c   T   : Cohesive traction vector
c   T_d : Derivative of the cohesive traction (Tangent matrix)
c   U_l : Nodal displacement in the local coordinate system
c   R   : Coordinate transformation matrix
c   Bc  : Global displacement-separation relation matrix
c   Bct : Transpose of Bc
c   ShapeN: Shape functional matrix
c   del : Normal and tangential separations
c   GP  : Gauss points
c   GP_W: Weight at the Gauss points
c   n_GP: Number of the Gauss points
      DOUBLE PRECISION Gn, Gt, Tn_m, Tt_m, alph, beta, ln, lt, th,
     & dn, dt, m, n, Gam_n, Gam_t, dGnt, dGtn,
     & N1, N2, del1, del2, del3, del4, deln_max, delt_max, el_length
c   Gn, Gt: Fracture energies
c   Tn_m, Tt_m: Cohesive strengths
c   alph, beta: Shape parameters
c   ln, lt: Initial slope indicators
c   th    : Thickness of a cohesive element
c   dn, dt: Final crack opening widths
c   m, n  : Exponents in the PPR potential
c   Gam_n, Gam_t: Energy constants in the PPR potential
c   dGnt  : <Gn - Gt>
c   dGtn  : <Gt - Gn>
c   N1, N2: Linear shape functions
c   del1, del2, del3, del4: Nodal separations
c   deln_max, delt_max: Maximum separations in a loading history
c   el_length: Length of a cohesive element
c ---------------------------------------------------------------------------
c Read input data & Initialize
      Gn   = PROPS(1)
      Gt   = PROPS(2)
      Tn_m = PROPS(3)
      Tt_m = PROPS(4)
      alph = PROPS(5)
      beta = PROPS(6)
      ln   = PROPS(7)
      lt   = PROPS(8)
```

```
      th   = PROPS(9)
      n_GP = 2
      data GP   / 0.577350269189626 , -0.577350269189626 /
      data GP_W / 1.0 , 1.0 /
      call k_Matrix_Zero (RHS,ndofel,nrhs)
      call k_Matrix_Zero (AMATRX,ndofel,ndofel)
c Determine the PPR parameters
      m = (alph-1)*alph*ln**2/(1-alph*ln**2)
      n = (beta-1)*beta*lt**2/(1-beta*lt**2)
      dn = alph*Gn/(m*Tn_m)*(1-ln)**(alph-1)
     &     * (alph/m*ln+1)**(m-1)*(alph+m)*ln
      dt = beta*Gt/(n*Tt_m)*(1-lt)**(beta-1)
     &     * (beta/n*lt+1)**(n-1)*(beta+n)*lt
      if (Gt .GT. Gn) then
         dGnt = 0
         dGtn = Gt - Gn
      elseif (Gt .LT. Gn) then
         dGnt = Gn - Gt
         dGtn = 0
      else
         dGnt = 0
         dGtn = 0
      endif
      if (Gn .EQ. Gt) then
         Gam_n = -Gn*(alph/m)**m
         Gam_t = (beta/n)**n
      else
         Gam_n = (-Gn)**(dGnt/(Gn-Gt))*(alph/m)**m
         Gam_t = (-Gt)**(dGtn/(Gt-Gn))*(beta/n)**n
      endif
c Change from the global coordinates to the local coordinates
      call k_Coords_Transform (R, el_length, COORDS, U, ndofel,
     & nnode, mcrd)
      do i = 0, nnode-1
         U_l(1+i*mcrd) = R(1,1)*U(1+i*mcrd) + R(1,2)*U(2+i*mcrd)
         U_l(2+i*mcrd) = R(2,1)*U(1+i*mcrd) + R(2,2)*U(2+i*mcrd)
      end do
      del1 = U_l(7) - U_l(1)
      del2 = U_l(8) - U_l(2)
      del3 = U_l(5) - U_l(3)
      del4 = U_l(6) - U_l(4)
c Numerical integration to compute RHS and AMATRX
      do i = 1, n_GP
         N1 = 0.5*(1 - GP(i))
         N2 = 0.5*(1 + GP(i))
         del(1) = N1*del1 + N2*del3
         del(2) = N1*del2 + N2*del4
         delt_max = SVARS(n_GP*(i-1)+1)
         deln_max = SVARS(n_GP*(i-1)+2)
         call k_Cohesive_PPR (T, T_d, Gam_n, Gam_t, alph, beta, m, n,
     &  dn, dt, dGtn, dGnt, del, deln_max, delt_max)
         ShapeN(1) = -N1
         ShapeN(2) = -N2
         ShapeN(3) = N2
         ShapeN(4) = N1
         do j = 1, nnode
            do k = 1, mcrd
              do l = 1, mcrd
                 Bc(k,l+(j-1)*mcrd) = ShapeN(j)*R(k,l)
              end do
```

```
            end do
          end do
          call k_Matrix_Transpose (Bc,Bct,mcrd,ndofel)
          call k_Matrix_Multiply (Bct,T_d,tmp,ndofel,mcrd,mcrd)
          call k_Matrix_Multiply (tmp,Bc,Sc,ndofel,mcrd,ndofel)
          call k_Matrix_Multiply (Bct,T,Fc,ndofel,mcrd,nrhs)
          thick = 0.5 * el_length * GP_w(i) * th
          call k_Matrix_PlusScalar (AMATRX,Sc,thick,ndofel,ndofel)
          call k_Matrix_PlusScalar (RHS,-Fc,thick,ndofel,nrhs)
c   Update the state variables: SVARS
          if ((delt_max.LT.abs(del(1))).AND.(abs(del(1)).GT.lt*dt)) then
            SVARS(n_GP*(i-1)+1) = abs(del(1))
          end if
          if ((deln_max .LT. del(2)) .AND. (del(2) .GT. ln*dn)) then
            SVARS(n_GP*(i-1)+2) = del(2)
          end if
        end do
        RETURN
        END
c
c ======================================================================
c = Cohesive traction-separation relation of the PPR model ==============
        SUBROUTINE k_Cohesive_PPR (T, T_d, Gam_n, Gam_t, alph, beta, m, n,
     &  dn, dt, dGtn, dGnt, del, deln_max, delt_max)
        INCLUDE 'ABA_PARAM.INC'
        DIMENSION T(2,1), T_d(2,2), del(2)
        DOUBLE PRECISION Gam_n, Gam_t, alph, beta, m, n, dn, dt,
     &    dGtn, dGnt, deln_max, delt_max, Tn, Tt, deln, delt, sign_dt
        delt = abs(del(1))
        deln = del(2)
        if (del(1) .GE. 0) then
          sign_dt = 1
        else
          sign_dt = -1
        end if
        Tn = 0
c Pre-calculation of the normal cohesive traction, Tn
        if (deln .LT. 0) then
          deln = 0
        elseif ((deln .GE. dn) .OR. (delt .GE. dt))  then
          Tn = 0
        elseif (deln .GE. deln_max) then
          Tn = (Gam_t*(1-delt/dt)**beta*(delt/dt+n/beta)**n+dGtn) *
     & Gam_n/dn*(m*(1-deln/dn)**alph*(m/alph+deln/dn)**(m-1)
     &      -alph*(1-deln/dn)**(alph-1)*(m/alph+deln/dn)**m)
        else
          Tn = (Gam_t*(1-delt/dt)**beta*(delt/dt+n/beta)**n+dGtn) *
     & Gam_n/dn*(m*(1-deln_max/dn)**alph*(m/alph+deln_max/dn)**(m-1)
     &   -alph*(1-deln_max/dn)**(alph-1)*(m/alph+deln_max/dn)**m) *
     & deln/deln_max
        end if
c Pre-calculation of the tangential cohesive traction, Tt
        if ((deln .GE. dn) .OR. (delt .GE. dt))  then
          Tt = 0
        elseif (delt .GE. delt_max) then
          Tt = (Gam_n*(1-deln/dn)**alph*(deln/dn+m/alph)**m+dGnt) *
     & Gam_t/dt*(n*(1-delt/dt)**beta*(delt/dt+n/beta)**(n-1)
     &      -beta*(1-delt/dt)**(beta-1)*(delt/dt+n/beta)**n)
        else
          Tt = (Gam_n*(1-deln/dn)**alph*(deln/dn+m/alph)**m+dGnt) *
```

```
     & Gam_t/dt*(n*(1-delt_max/dt)**beta*(delt_max/dt+n/beta)**(n-1)
     &   -beta*(1-delt_max/dt)**(beta-1)*(delt_max/dt+n/beta)**n) *
     & delt/delt_max
       end if
c Normal cohesive interaction
c   (1) Contact condition
       if (del(2). LT. 0) then
          T_d(2,2) = -Gam_n/dn**2*(m/alph)**(m-1)*(alph+m)*
     & (Gam_t*(n/beta)**n + dGtn)
          T_d(2,1) = 0
          T(2,1) = T_d(2,2)*del(2)
       else if ((deln.LT.dn).AND.(delt.LT.dt).AND.(Tn.GE.-1.0E-5)) then
          T(2,1) = Tn
c   (2) Softening condition
          if (deln .GE. deln_max) then
             T_d(2,2) =
     & (Gam_t*(1-delt/dt)**beta*(delt/dt+n/beta)**n+dGtn) *
     & Gam_n/dn**2 *
     & ((1-deln/dn)**(alph-2)*(alph-1)*alph*(deln/dn+m/alph)**m -
     & 2*(1-deln/dn)**(alph-1)*alph*(deln/dn+m/alph)**(m-1)*m +
     & (1-deln/dn)**alph*(deln/dn+m/alph)**(m-2)*(m-1)*m)
             T_d(2,1) =
     & Gam_t/dt*(-(1-delt/dt)**(beta-1)*beta*(delt/dt+n/beta)**n +
     & (1-delt/dt)**beta*(delt/dt+n/beta)**(n-1)*n) * sign_dt *
     & Gam_n/dn*(-(1-deln/dn)**(alph-1)*alph*(deln/dn+m/alph)**m +
     & (1-deln/dn)**alph*(deln/dn+m/alph)**(m-1)*m)
c   (3) Unloading/reloading condition
          else
             T_d(2,2) =
     & (Gam_t*(1-delt/dt)**beta*(delt/dt+n/beta)**n+dGtn) *
     & Gam_n/dn*((1-deln_max/dn)**alph*(deln_max/dn+m/alph)**(m-1)*m
     & -(1-deln_max/dn)**(alph-1)*alph*(deln_max/dn+m/alph)**m)
     & / deln_max
             T_d(2,1) =
     & Gam_t/dt*(-(1-delt/dt)**(beta-1)*beta*(delt/dt+n/beta)**n +
     & (1-delt/dt)**beta*(delt/dt+n/beta)**(n-1)*n) * sign_dt *
     & Gam_n/dn*(m*(1-deln_max/dn)**alph*(m/alph+deln_max/dn)**(m-1)
     &   -alph*(1-deln_max/dn)**(alph-1)*(m/alph+deln_max/dn)**m) *
     & deln/deln_max
          end if
c   (4) Complete failure condition
       else
          T(2,1) = 0
          T_d(2,2) = 0
          T_d(2,1) = 0
       endif
c Tangential cohesive interaction
       if ((delt.LT.dt) .AND. (deln.LT.dn) .AND. (Tt.GE.-1.0E-5)) then
          T(1,1) = Tt*sign_dt
c   (1) Softening condition
          if (delt .GE. delt_max) then
             T_d(1,1) =
     & (Gam_n*(1-deln/dn)**alph*(deln/dn+m/alph)**m+dGnt) *
     & Gam_t/dt**2 *
     & ((1-delt/dt)**(beta-2)*(beta-1)*beta*(delt/dt+n/beta)**n -
     & 2*(1-delt/dt)**(beta-1)*beta*(delt/dt+n/beta)**(n-1)*n +
     & (1-delt/dt)**beta*(delt/dt+n/beta)**(n-2)*(n-1)*n)
             T_d(1,2) =
     & Gam_t/dt*(-(1-delt/dt)**(beta-1)*beta*(delt/dt+n/beta)**n +
     & (1-delt/dt)**beta*(delt/dt+n/beta)**(n-1)*n) * sign_dt *
```

```
     & Gam_n/dn*(-(1-deln/dn)**(alph-1)*alph*(deln/dn+m/alph)**m +
     & (1-deln/dn)**alph*(deln/dn+m/alph)**(m-1)*m)
c   (2) Unloading/reloading condition
         else
            T_d(1,1) =
     & (Gam_n*(1-deln/dn)**alph*(deln/dn+m/alph)**m+dGnt) *
     & Gam_t/dt*(n*(1-delt_max/dt)**beta*(delt_max/dt+n/beta)**(n-1)
     &     -beta*(1-delt_max/dt)**(beta-1)*(delt_max/dt+n/beta)**n)
     & / delt_max
            T_d(1,2) =
     & Gam_n/dn*(-(1-deln/dn)**(alph-1)*alph*(deln/dn+m/alph)**m +
     & (1-deln/dn)**alph*(deln/dn+m/alph)**(m-1)*m) * sign_dt *
     & Gam_t/dt*(n*(1-delt_max/dt)**beta*(delt_max/dt+n/beta)**(n-1)
     &   -beta*(1-delt_max/dt)**(beta-1)*(delt_max/dt+n/beta)**n) *
     & delt/delt_max
         end if
c   (3) Complete failure condition
       else
          T(1,1) = 0
          T_d(1,1) = 0
          T_d(1,2) = 0
       endif
c      if (T_d(1,2) .NE. T_d(2,1)) then
c         T_d(1,2) = 0.5*(T_d(1,2) + T_d(2,1))
c         T_d(2,1) = T_d(1,2)
c      endif
       RETURN
       END
c
c ======================================================================
c = Coordinate Transformation ========================================
c   : Coordinate transformation matrix (R) is obtained on the basis of
c   the deformed configuration
       SUBROUTINE k_Coords_Transform (R, el_length, COORDS, U, ndofel,
     & nnode, mcrd)
       INCLUDE 'ABA_PARAM.INC'
       DIMENSION R(mcrd,mcrd), COORDS(mcrd,nnode), U(ndofel)
       DIMENSION Co_de(mcrd,nnode), Co_de_m(2,2)
c Variables used in the k_Coords_Transform subroutine
c   Co_de  : Coord. of a cohesive element in the deformed configuration
c   Co_de_m: Mid-points of a cohesive element to compute the orientation
c   el_length: length of a cohesive element
c
       do i = 1, mcrd
          do j = 1, nnode
             Co_de(i,j) = COORDS(i,j) + U(2*(j-1)+i)
          end do
       end do
       do i = 1, 2
          Co_de_m(i,1) = (Co_de(i,1)+Co_de(i,4))*0.5
          Co_de_m(i,2) = (Co_de(i,2)+Co_de(i,3))*0.5
       end do
c Calculate the directional cosine & the transformation matrix
       d_x = Co_de_m(1,2) - Co_de_m(1,1)
       d_y = Co_de_m(2,2) - Co_de_m(2,1)
       el_length = (d_x**2 + d_y**2)**0.5
       cos_a = d_x / el_length
       sin_a = d_y / el_length
       R(1,1) = cos_a
       R(1,2) = sin_a
```

```
      R(2,1) = -sin_a
      R(2,2) = cos_a
      RETURN
      END
c
c ======================================================================
c = Matrix operations ================================================
      SUBROUTINE k_Matrix_Zero (A,n,m)
      INCLUDE 'ABA_PARAM.INC'
      DIMENSION A(n,m)
      do i = 1, n
         do j = 1, m
            A(i,j) = 0.0
         end do
      end do
      RETURN
      END
c
      SUBROUTINE k_Matrix_Transpose (A,B,n,m)
      INCLUDE 'ABA_PARAM.INC'
      DIMENSION A(n,m), B(m,n)
      call k_Matrix_zero (B,m,n)
      do i = 1, n
         do j = 1, m
            B(j,i) = A(i,j)
         end do
      end do
      RETURN
      END
c
      SUBROUTINE k_Matrix_PlusScalar (A,B,c,n,m)
      INCLUDE 'ABA_PARAM.INC'
      DIMENSION A(n,m), B(n,m)
      do i = 1, n
         do j = 1, m
            A(i,j) = A(i,j) + c*B(i,j)
         end do
      end do
      RETURN
      END
c
      SUBROUTINE k_Matrix_Multiply (A,B,C,l,n,m)
      INCLUDE 'ABA_PARAM.INC'
      DIMENSION A(l,n), B(n,m), C(l,m)
      call k_Matrix_zero (C,l,m)
      do i = 1, l
         do j = 1, m
            do k = 1, n
              C(i,j) = C(i,j) + A(i,k) * B (k,j)
            end do
         end do
      end do
      RETURN
      END
c ======================================================================
```

References

[1] Park K. Potential-based fracture mechanics using cohesive zone and virtual internal bond modeling. PhD Thesis, University of Illinois at Urbana-Champaign; 2009.
[2] Anderson TL. Fracture mechanics: fundamentals and applications. Boca Raton: CRC Press; 1995.
[3] Barenblatt GI. The formation of equilibrium cracks during brittle fracture: general ideas and hypotheses, axially symmetric cracks. Appl Math Mech 1959;23(3):622–36.
[4] Dugdale DS. Yielding of steel sheets containing slits. J Mech Phys Solids 1960;8(2):100–4.
[5] Hillerborg A, Modeer M, Petersson PE. Analysis of crack formation and crack growth in concrete by means of fracture mechanics and finite elements. Cement Concr Res 1976;6(6):773–81.
[6] Boone TJ, Wawrzynek PA, Ingraffea AR. Simulation of the fracture process in rock with application to hydrofracturing. Int J Rock Mech Min Sci 1986;23(3):255–65.
[7] Bazant ZP, Planas J. Fracture and size effect in concrete and other quasibrittle materials. Boca Raton: CRC Press; 1998.
[8] Park K, Paulino GH, Roesler JR. Determination of the kink point in the bilinear softening model for concrete. Engng Fract Mech 2008;75(13):3806–18.
[9] Ingraffea AR, Gerstle WH, Gergely P, Saouma V. Fracture mechanics of bond in reinforced concrete. J Struct Engng 1984;110(4):871–90.
[10] Xu C, Siegmund T, Ramani K. Rate-dependent crack growth in adhesives: I. Modeling approach. Int J Adhes Adhes 2003;23(1):9–13.
[11] Matous K, Kulkarni MG, Geubelle PH. Multiscale cohesive failure modeling of heterogeneous adhesives. J Mech Phys Solids 2008;56(4):1511–33.
[12] Xu XP, Needleman A. Void nucleation by inclusion debonding in a crystal matrix. Modell Simul Mater Sci Engng 1993;1(2):111–32.
[13] Ngo D, Park K, Paulino GH, Huang Y. On the constitutive relation of materials with microstructure using a potential-based cohesive model for interface interaction. Engng Fract Mech 2010;77(7):1153–74.
[14] Needleman A, Borders TL, Brinson L, Flores VM, Schadler LS. Effect of an interphase region on debonding of a CNT reinforced polymer composite. Compos Sci Technol 2010;70(15):2207–15.
[15] Park K, Paulino GH, Roesler JR. A unified potential-based cohesive model of mixed-mode fracture. J Mech Phys Solids 2009;57(6):891–908.
[16] ABAQUS. Version 6.2. H.K.S. Pawtucket: Hibbitt, Karlsson & Sorensen; 2002.
[17] Sigmund O. A 99 line topology optimization code written in Matlab. Struct Multidisc Optimiz 2001;21(2):120–7.
[18] Giner E, Sukumar N, Tarancon JE, Fuenmayor FJ. An ABAQUS implementation of the extended finite element method. Engng Fract Mech 2009;76(3):347–68.
[19] Ortiz M, Pandolfi A. Finite-deformation irreversible cohesive elements for three-dimensional crack-propagation analysis. Int J Numer Meth Engng 1999;44(9):1267–82.
[20] Zhang Z, Paulino GH, Celes W. Extrinsic cohesive modelling of dynamic fracture and microbranching instability in brittle materials. Int J Numer Meth Engng 2007;72(8):893–923.
[21] Wells GN, Sluys LJ. A new method for modelling cohesive cracks using finite elements. Int J Numer Meth Engng 2001;50(12):2667–82.
[22] Moes N, Belytschko T. Extended finite element method for cohesive crack growth. Engng Fract Mech 2002;69(7):813–33.
[23] Simo JC, Oliver J, Armero F. An analysis of strong discontinuities induced by strain-softening in rate-independent inelastic solids. Comput Mech 1993;12(5):277–96.
[24] Oliver J, Huespe AE, Pulido MDG, Chaves E. From continuum mechanics to fracture mechanics: the strong discontinuity approach. Engng Fract Mech 2002;69(2):113–36.
[25] Linder C, Armero F. Finite elements with embedded strong discontinuities for the modeling of failure in solids. Int J Numer Meth Engng 2007;72(12):1391–433.
[26] Klein PA, Foulk JW, Chen EP, Wimmer SA, Gao HJ. Physics-based modeling of brittle fracture: cohesive formulations and the application of meshfree methods. Theor Appl Fract Mech 2001;37(1–3):99–166.
[27] Roesler J, Paulino GH, Park K, Gaedicke C. Concrete fracture prediction using bilinear softening. Cem Concr Compos 2007;29(4):300–12.
[28] Roe KL, Siegmund T. An irreversible cohesive zone model for interface fatigue crack growth simulation. Engng Fract Mech 2003;70(2):209–32.
[29] Reeder JR, Crews Jr JH. Mixed-mode bending method for delamination testing. AIAA J 1990;28(7):1270–6.
[30] Mi Y, Crisfield MA, Davies GAO, Hellweg HB. Progressive delamination using interface elements. J Compos Mater 1998;32(14):1246–72.
[31] Crisfield MA. A fast incremental/iterative solution procedure that handles snap-through. Comput Struct 1981;13(1-3):55–62.
[32] Tan H, Liu C, Huang Y, Geubelle PH. The cohesive law for the particle/matrix interfaces in high explosives. J Mech Phys Solids 2005;53(8):1892–917.
[33] Zhang Z, Paulino GH. Cohesive zone modeling of dynamic failure in homogeneous and functionally graded materials. Int J Plast 2005;21(6):1195–254.